

## Supporting information

### Environmentally Responsive Hydrogel Composites for Dynamic Body Thermoregulation

M. Garzón Altamirano<sup>a,b</sup>, M. G. Abebe<sup>c</sup>, N. Hergué<sup>a</sup>, J. Lejeune<sup>b</sup>, A. Cayla<sup>b</sup>, C. Campagne<sup>b</sup>, B. Maes<sup>c</sup>, E. Devaux<sup>b</sup>, J. Odent<sup>a\*</sup>, J.M Raquez<sup>a</sup>

- a. Laboratory of Polymeric and Composite Materials (LPCM), Center of Innovation and Research in Materials and Polymers (CIRMAP), University of Mons (UMONS), Mons, Belgium.
- b. University of Lille, ENSAIT, ULR 2461 – GEMTEX – Génie et Matériaux Textiles, F-59000 Lille, France.
- c. Micro- and Nanophotonic Materials Group, Research Institute for Materials Science and Engineering University of Mons, 20 Place du Parc, B-7000, Mons, Belgium.
- \* E-mail: jeremy.odent@umons.ac.be

**Table S1.** Physicochemical properties, LCST behavior and morphology

Sample	Gel fraction (%)	Swelling ratio (%)	LCST (°C)
0% SiO <sub>2</sub>	91.0 ± 0.9	835.6 ± 23.5	35.4 ± 0.1
5% SiO <sub>2</sub>	90.8 ± 0.6	696.6 ± 11.0	35.5 ± 0.1
10% SiO <sub>2</sub>	91.0 ± 0.5	675.3 ± 6.20	35.1 ± 0.1
20% SiO <sub>2</sub>	90.8 ± 0.4	645.1 ± 2.30	34.8 ± 0.2
30% SiO <sub>2</sub>	91.0 ± 0.4	632.2 ± 5.00	34.3 ± 0.1
40% SiO <sub>2</sub>	91.4 ± 0.1	511,4 ± 8.10	34.0 ± 0.1

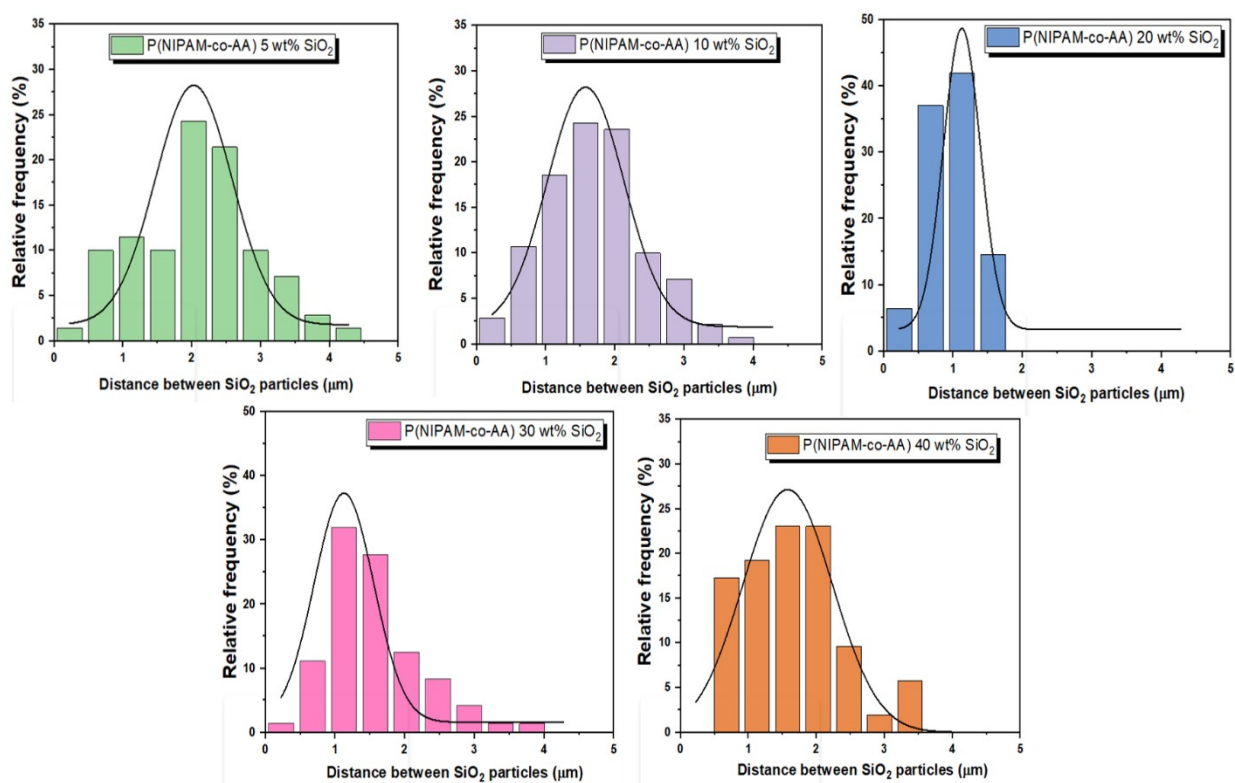


**Figure S1.** Distance distribution of SiO<sub>2</sub> particles in the hydrogel composite.

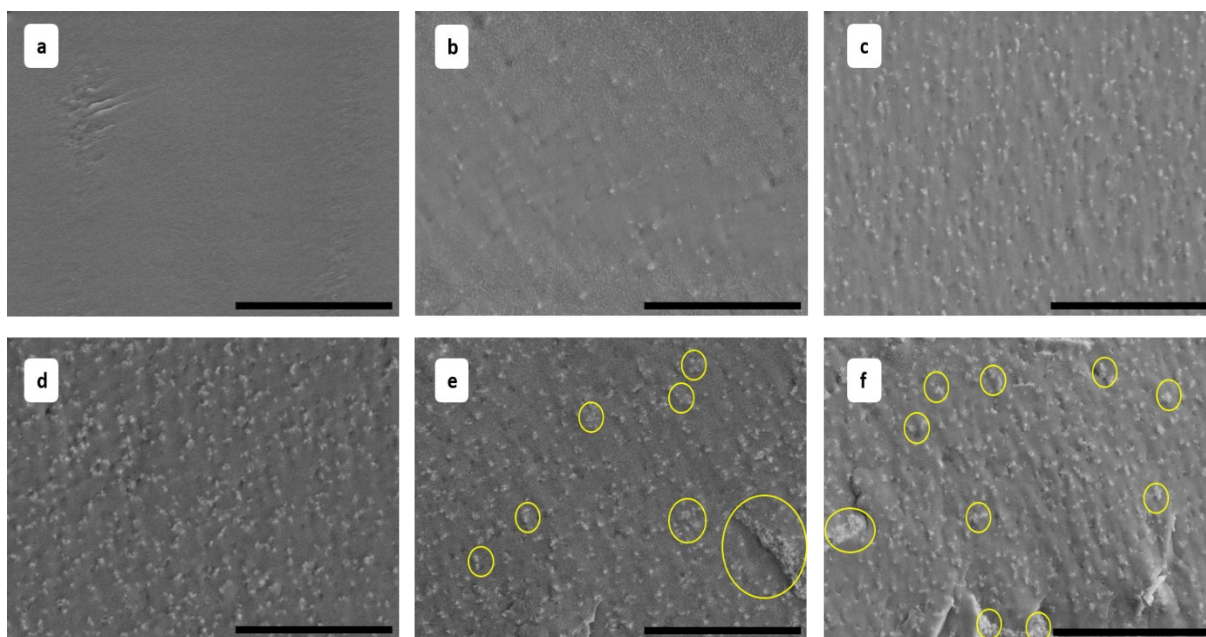


**Figure S2.** SEM Images: Dispersion of silica particles on the hydrogel composite. (a) 0%, (b) 5%, (c) 10%, (d) 20%, (e) 30% and (f) 40 wt% SiO<sub>2</sub> respectively. Scale bar 10 $\mu$ m. Agglomeration at higher concentration of SiO<sub>2</sub> highlighted using yellow circles

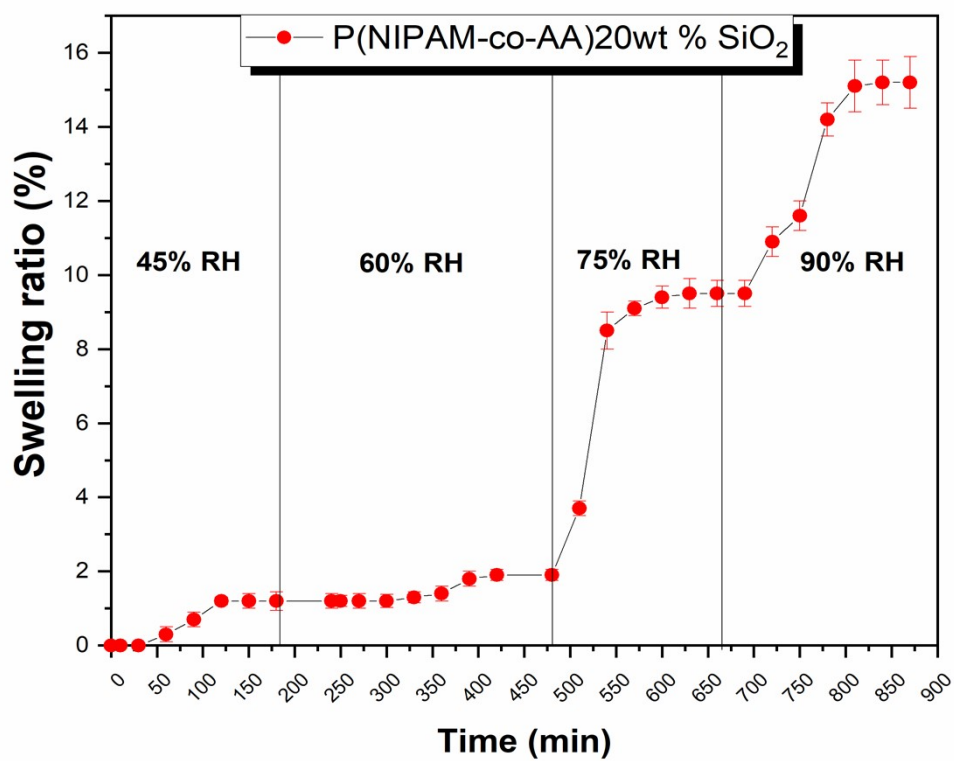


**Figure S3.** Swelling kinetics of the hydrogel composite at each level of relative humidity

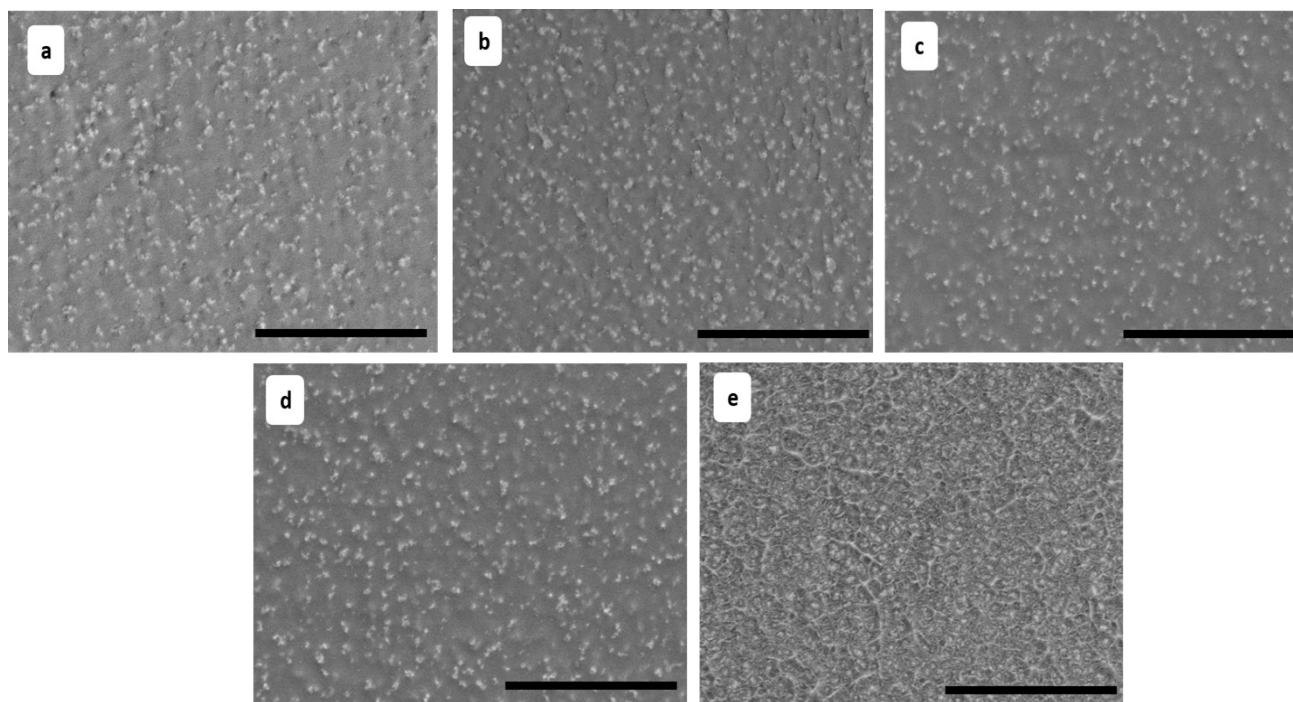


**Figure S4.** SEM Images: Dispersion of silica particles in the hydrogel composite for different levels of relative humidity at 20°C. (a) 0% (b) 45%, (c) 60%, (d) 75%, and (e) 90% RH respectively. Scale bar 10μm

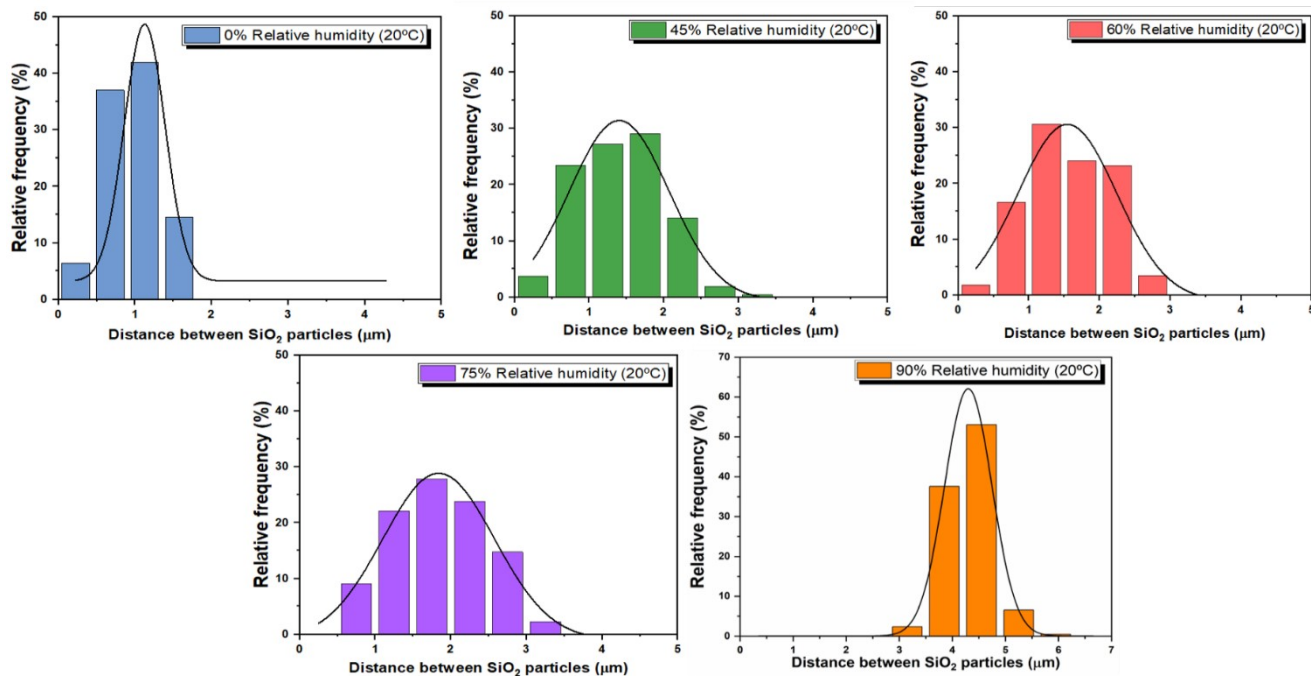


**Figure S5.** Distance distribution of SiO<sub>2</sub> particles in the composite hydrogel at different humidity levels.

**Table S2.** Data of area values between 5-15  $\mu\text{m}$  for different effects on hydrogels composite

$$\int_{\lambda_1}^{\lambda_2} \phi_{bb}(\lambda) d\lambda$$

<b>Human body emissivity</b>		810.99	100
<b>Sample</b>		$\int_{\lambda_1}^{\lambda_2} R(\lambda)\phi_{bb}(\lambda) d\lambda$	$\rho$ (%) *
<b>wt% SiO<sub>2</sub></b> Dry samples 20°C	0	34.42	4.2
	5	62.07	7.7
	10	86.29	10.6
	20	166.67	20.6
	30	112.37	13.9
	40	94.83	11.7
<b>Relative humidity (%)</b> 20°C	0	166.67	20.6
	45	218.62	27.0
	60	243.29	30.0
	75	199.89	24.6
	90	137.9	17.0
	75	211.15	26.0
	60	244.35	30.1
	45	230.86	28.5
<b>Temperature (°C)</b> 60% RH	20	243.29	30.0
	30	282.24	34.8
	35	344.14	42.4
	40	228.17	28.1
	50	208.83	25.8

**Table S3.** Roughness values of P(NIPAM-co-AA)/20wt% SiO<sub>2</sub> films as a function of relative humidity. Temperature constant 20°C

Relative humidity (%) (20°C)	Ra (μm)*	Rq (μm)*
0	16.80 ± 3.14	20.38 ± 5.28
45	15.45 ± 2.29	18.95 ± 5.92
60	13.53**	17.51**
75	11.45 ± 1.45	16.15 ± 3.32
90	5.80 ± 2.58	6.75 ± 3.27

\*Values determine by averaged over 6 roughness measurements of each surface of the prepared samples.

\*\* Values determine by 3D roughness analysis

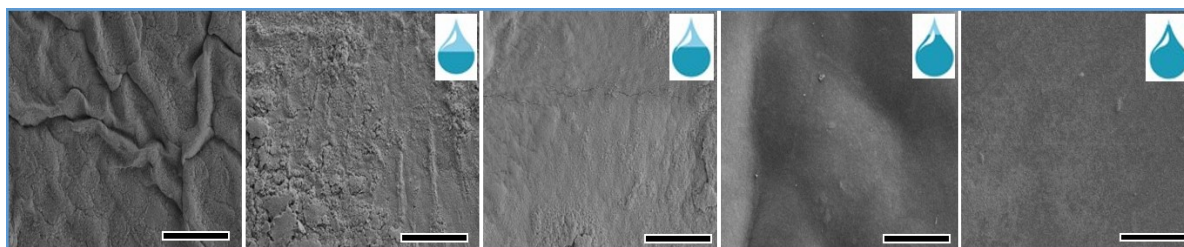


**Figure S6.** SEM images: Changes in the surface morphology of the hydrogel composite containing 20 wt.% of SiO<sub>2</sub> when subjected to different humidity levels. From left to right 0%, 45%, 60%, 75% and 90% RH. Scale bar 50μm

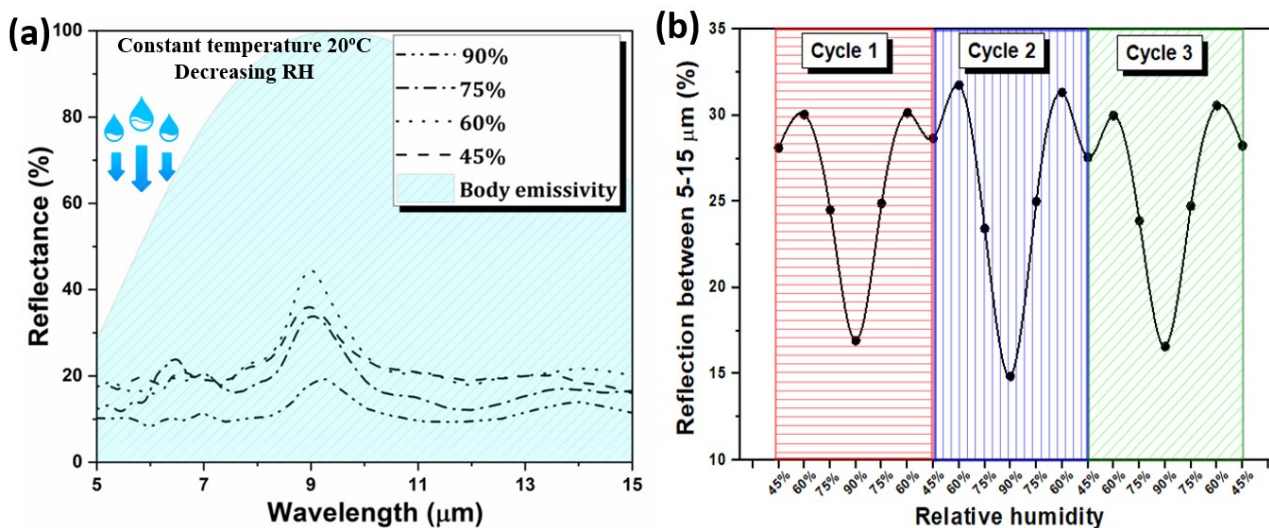


**Figure S7.** Infrared spectra of the P(nipam-co-AA) hydrogels charged with 20wt% SiO<sub>2</sub> particles. Reflection of infrared radiation emitted by the human body at 34°C. Effect of relative humidity on P(nipam-co-AA) + 20%SiO<sub>2</sub> (a) Decreasing relative humidity (b) Trend of the dynamic behavior of hydrogel composite against composite infrared radiation when applying continuous humidity cycles

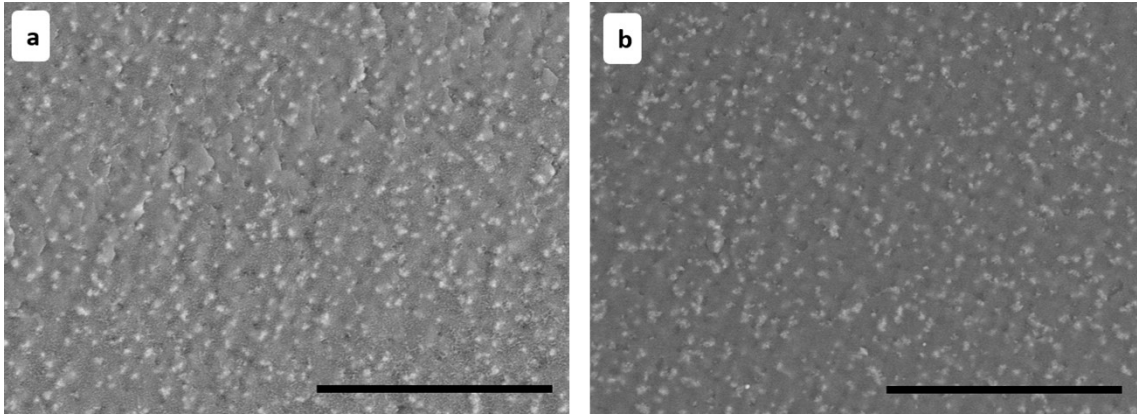


**Figure S8.** SEM Images: Dispersion of silica particles in the hydrogel composite at different temperatures at 60%RH. (a) 35°C and (b) 50°C. Scale bar 10 $\mu$ m.

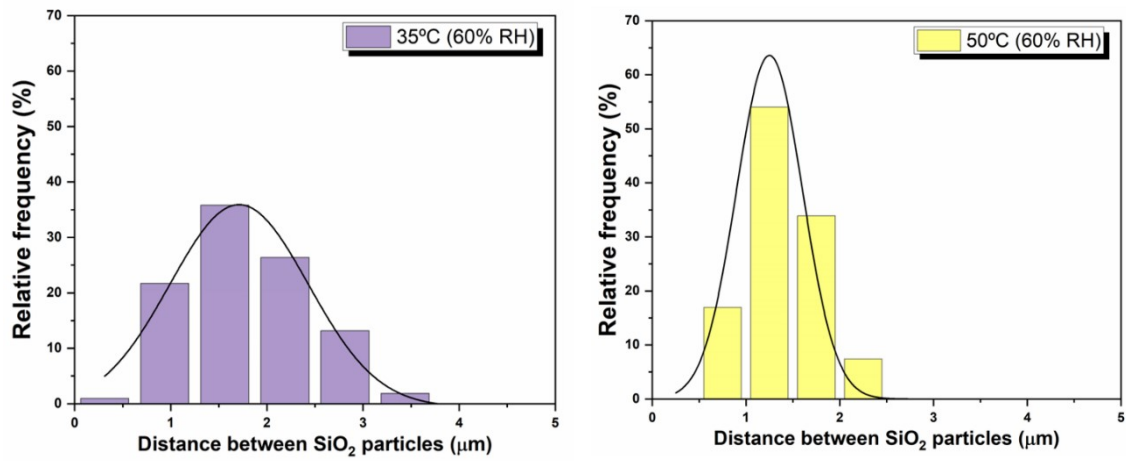


**Figure S9.** Distance distribution of SiO<sub>2</sub> particles in the composite hydrogel at different temperatures at 60%RH

**Table S4.** Roughness values of P(NIPAM-co-AA)/20wt% SiO<sub>2</sub> films as a function of temperature. 60%RH

		<b>Ra (μm)*</b>	<b>Rq (μm)*</b>
Temperature (°C) (60% RH)	20	13.53	17.51
	35	8.37	9.79
	50	14.2	14.95

\*Values determine by 3D roughness analysis

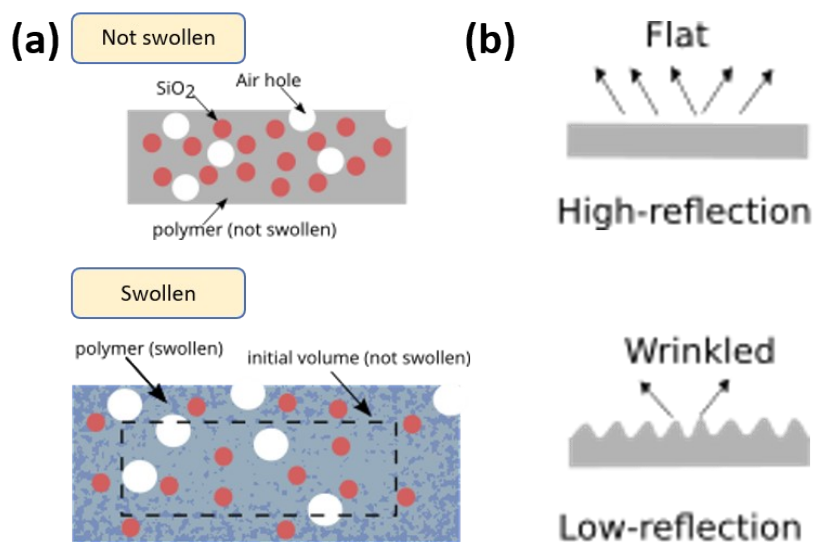


**Figure S11.** (a) Theoretical scheme of the change in volume of the hydrogel composite together with change in the distribution of SiO<sub>2</sub> particles with respect to the relative humidity. (b) Theoretical scheme of the change in the surface morphology of the hydrogel composite with respect to the temperature.

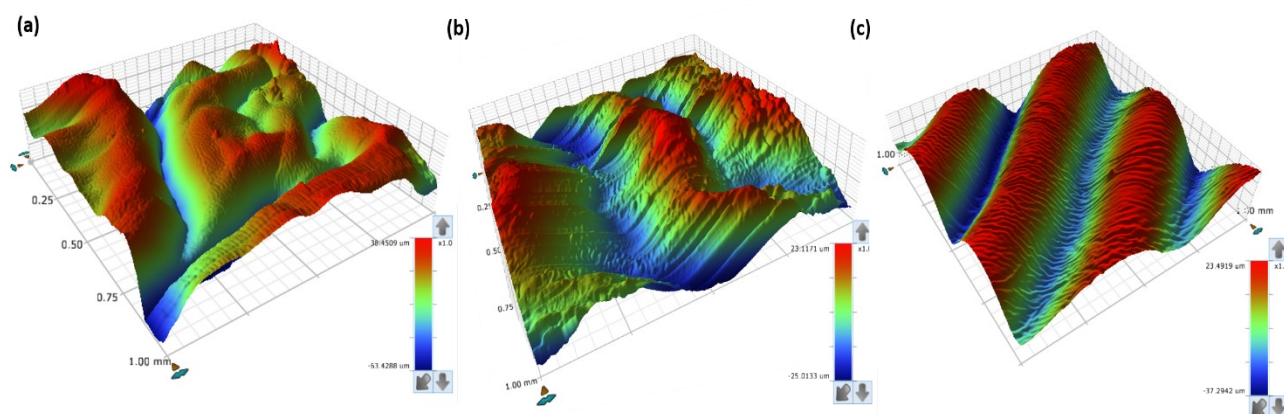


**Figure S10.** Surface Images by DEKTAK, rough profile of P(NIPAM-co-AA) surfaces at different humidities at 60%RH. (a) 20°C, (b) 35°C, (c) 50°C

## Modeling optical properties of particle clouds

The radiative properties of an ensemble of particles randomly dispersed in a polymer matrix can be modeled using the extended version of Lorenz-Mie solutions. For independent scattering, spherical particles with radius  $r_i$  and volume fraction  $f_{v,i}$  dispersed in a matrix, the fraction of energy scattered by all the particles (per unit length along the direction of the incoming electromagnetic wave) is equal to the scattering cross section ( $Q_{sca,i}$ ) summed over all particles. Thus, one obtains the effective scattering coefficient:

$$\sigma_{\text{eff}} = \sum_{i=1}^m \frac{3f_{v,i}}{4r_i} Q_{sca,i}$$

and the effective absorption coefficient:

$$\kappa_{\text{eff}} = \sum_{i=1}^m \frac{3f_{v,i}}{4r_i} Q_{abs,i}$$

Here  $Q_{abs,i}$  is the absorption cross section. The effective extinction coefficient ( $\beta_{\text{eff}}$ ) is calculated by summing the effective absorption and scattering coefficients. The expressions can be used for several types of inclusions, indexed by  $i$ , but here we use uniform particles with fixed size - therefore, the summations disappear.

## Radiative transfer modeling using Monte Carlo method

Radiative transport through the composite fabric can be modeled using the conventional radiative transfer equation (RTE). We consider the fabric as a homogeneous slab medium, and employ the effective radiative quantities computed as an input to solve the RTE. Subsequently, the fabric's important radiative transport qualities (*i.e.* reflection) in the human body emission band are retrieved.

$$\frac{dI}{ds} = \kappa_{\text{eff}} I_{\text{bb}} - \beta_{\text{eff}} I + \frac{\sigma_{\text{eff}}}{4\pi} \int I \Phi(\Omega', \Omega) d\Omega'$$

with  $I$  the radiative intensity field,  $s$  the path length,  $I_{\text{bb}}$  the blackbody intensity, and  $\Phi(\Omega', \Omega)$  the scattering phase function, which describes the distribution of scattered energy coming from direction  $\Omega'$  into direction  $\Omega$  with the scattering angle between the two directions. The first term on the right-hand side represents the emission, the second term represents extinction due to absorption and scattering, the last term denotes radiation augmentation due to in-scattering.

Due to its accuracy and simplicity, the Monte Carlo (MC) method is chosen for this study (Fig. S11a). We implement the extended version of collision-based forward MC method algorithm used by Abebe *et al.*<sup>49</sup>. This algorithm's main advantage is to capitalize on the parallelization possibility and to utilize a Graphics processing unit (GPU) accelerator, allowing to launch tens of thousands of photons and to retrieve results in reasonably short times. About 105 photons are launched for 30 angles (from 0° to 90°) and 24701 wavelengths (from 5 to 15  $\mu\text{m}$ ). Therefore, approximately  $7.4 \times 10^9$  photons are launched to calculate reflection. A short description of the MC process: a photon is launched at the upper boundary of the fabric for each run, with a certain propagation direction. The photon moves until it is reflected by the fabric. During each step, the photon travels a random distance with mean equal to the photon's path-length in the medium. When scattering occurs, the new propagation direction is determined via the scattering phase function. When photons strike the fabric interface, a fraction of them will be reflected, and the rest will be refracted. The entrance angle for photon tracing is handled using Snell's law. Specular reflectance at the

boundaries is computed using the conventional Fresnel equations which depends on the volume fraction of the composite.

### Modeling flat and wrinkled surfaces

In order to study the IR radiative response of the design, we utilize a commercial finite-element-based Maxwell equations solver (COMSOL Multiphysics). The wrinkled structure has a height  $h = 5 \mu\text{m}$  and period  $d = 4 \mu\text{m}$ . These values are taken for an optimized geometry. Simulations are performed for normal incident radiation with two polarizations, *i.e.* Transverse Electric (TE) and Transverse Magnetic (TM). Floquet periodic boundary conditions are used in the vertical direction to mimic the periodicity. Furthermore, all diffraction orders are included by implementing a port condition on the right and left side of the fabric model in COMSOL (Fig. S10b).

### Thermal modeling

The cooling and heating performance is assessed with the ambient setpoint temperature, which is determined from a heat transfer analysis using a thermal circuit model. We treated the thermal dissipation from the human body to the ambient as a 1D steady-state heat transfer problem in dry conditions. Using this analogy, the three heat transfer channels, when the fabric covers the skin with an air gap in between, are radiation, conduction, and convection (Fig. S11b).

For a semi-transparent, (absorbing and emitting) fabric layer, radiative ( $Q_{\text{rad,air}}$ ) and conductive ( $Q_{\text{cond,air}}$ ) heat transfer processes constitute the exchange through the air gap, while the heat dissipation from the fabric to the ambient is via radiation ( $Q_{\text{rad,amb}}$ ) and convection exchanges ( $Q_{\text{rad,conv}}$ ). Conductive exchange ( $Q_{\text{cond,tex}}$ ) contributes to the heat transfer in the textile. Furthermore, radiation ( $Q_{\text{rad,tran}}$ ) exchange occurs between the skin and the ambient with transmission through the fabric layer. When the transmission through the fabric is low, one can assume an opaque layer, so  $Q_{\text{rad,tran}} = 0$ . Note that the assumption that the convective heat transfer in the air gap is negligible also holds for this design. Indeed, this is due to the small Rayleigh number, which stems from the relatively small air gap thickness. The corresponding thermal circuit model is constructed with thermal resistances (Fig. S11c) where  $T_{\text{skin}}$  and  $\epsilon_s$  are the skin temperature and skin emissivity.  $T_{\text{amb}}$  and  $\epsilon_a$  are the ambient temperature and ambient emissivity.  $T_{\text{in}}$  is the inner and  $T_{\text{out}}$  the outer textile surface temperature, and  $\epsilon_t$  is textile emissivity.  $R_{\text{rad,air}}$  and  $R_{\text{cond,air}}$  are the radiative and conduction thermal resistances of air.  $R_{\text{cond,tex}}$  is the textile conductive thermal resistance,  $R_{\text{rad,tran}}$  the thermal resistance of radiative transmission,  $R_{\text{rad,amb}}$  the radiative thermal resistance of ambient, and  $R_{\text{conv}}$  the convective thermal resistance. The requirement for a wearer's thermal comfort is the balance between metabolic heat generation ( $Q_{\text{gen}}$ ) and total heat loss in dry conditions ( $Q_{\text{dry}}$ ). The total heat loss is controlled by the total thermal resistance  $R_{\text{tot}}$  between skin and ambient. The total heat flux through the air gap and fabric to the ambient is given by:

$$Q_{\text{gen}} = Q_{\text{dry}} = \frac{T_{\text{skin}} - T_{\text{amb}}}{R_{\text{tot}}}.$$

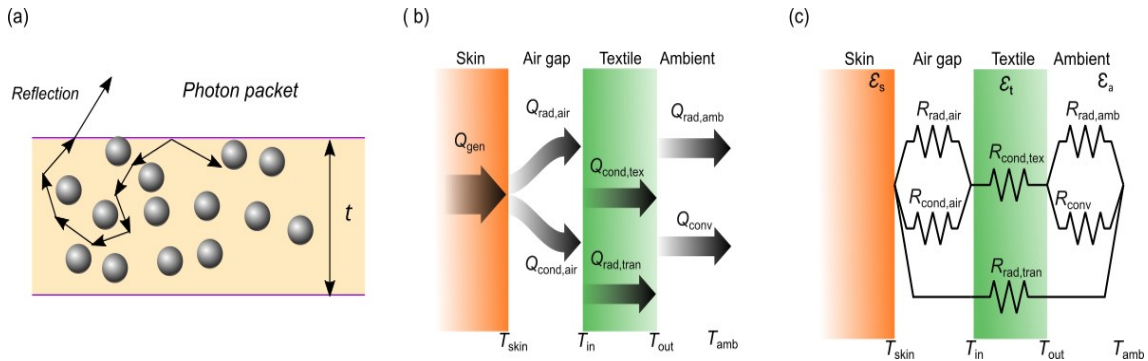


**Figure S12.** Schematic representation of (a) Monte Carlo method, (b) the different heat transfer channels, and (c) thermal circuit model.